TIMED Doppler Interferometer: Overview and recent results

T. L. Killeen,[1] Q. Wu,[1] S. C. Solomon,[1] D. A. Ortland,[2] W. R. Skinner,[3] R. J. Niciejewski,[3] and D. A. Gell[3]

[1]   The Thermosphere-Ionosphere-Mesosphere Energetics and Dynamics (TIMED) satellite carries a limb-scanning Fabry-Perot interferometer designed to perform remote-sensing measurements of upper atmosphere winds and temperatures globally. This instrument is called the TIMED Doppler Interferometer, or TIDI. This paper provides an overview of the TIDI instrument design, on-orbit performance, operational modes, data processing and inversion procedures, and a summary of wind results to date. Daytime and nighttime neutral winds in the mesosphere and lower thermosphere/ionosphere (MLTI) are measured on TIDI using four individual scanning telescopes that collect light from various upper atmosphere airglow layers on both the cold and warm sides of the high-inclination TIMED spacecraft. The light is spectrally analyzed using an ultrastable plane etalon Fabry-Perot system with sufficient spectral resolution to determine the Doppler line characteristics of atomic and molecular emissions emanating from the MLTI. The light from all four telescopes and from an internal calibration field passes through the etalon and is combined on a single image plane detector using a Circle-to-Line Interferometer Optic (CLIO). The four geophysical fields provide orthogonal line-of-sight measurements to either side of the satellite's path and these are analyzed to produce altitude profiles of vector winds in the MLTI. The TIDI wind measurements presented here are from the molecular oxygen (0-0) band, covering the altitude region 85–105 km. The unique TIDI design allows for more extended local time coverage of wind structures than previous wind-measuring instruments from high-inclination satellites. The TIDI operational performance has been nominal except for two anomalies: (1) higher than expected background white light caused by a low-level light leak and (2) ice deposition on cold optical surfaces. Both anomalies are well understood and the instrumental modes and data analysis techniques have been adjusted to mitigate their effects on data quality. The analysis techniques used to derive winds are described. The TIDI wind measurements from multiple yaw cycles of TIMED have been used to extract migrating diurnal and semidiurnal tides. The migrating tide results are compared with predictions from the Global Scale Wave Model (GSWM), and results from the Upper Atmospheric Research Satellite, High Resolution Doppler Imager (HRDI) instrument. TIDI wind measurements are also compared with ground-based meteor radar observations, showing consistent results.

1.   Introduction

[2]   A major objective of the NASA Thermosphere-Ionosphere-Mesosphere Energetics and Dynamics (TIMED) mission involves study of the global wind and temperature structure of the mesosphere and lower thermosphere-iono-sphere (MTLI) region of the terrestrial atmosphere. The TIMED Doppler Interferometer (TIDI), one of four complementary instruments on the spacecraft, is designed to carry out remote sensing measurements of the vector wind and temperature profiles through direct observations of the Doppler line and band characteristics of naturally occurring atmospheric emissions emanating from the MLTI. This paper describes the TIDI instrument design, summarizes its orbital performance, and presents recent results from analysis of the observed global wind fields. The dynamics of the MLTI have been the focus of many observational and modeling studies, and previous observations from satellite and ground-based instrumentation have considerably expanded our knowledge of this region.

[1]National Center for Atmospheric Research, High Altitude Observatory, Boulder, Colorado, USA.
[2]Northwest Research Associates, Bellevue, Washington, USA.
[3]Space Physics Research Laboratory, University of Michigan, Ann Arbor, Michigan, USA.

[3] A long history of ground-based observations of winds using the 557.7 nm emission at ∼97 km and OH emission lines at ∼86 km altitude has been created [e.g., *Hernandez and Smith*, 1984; *Cogger et al.*, 1985; *Wiens et al.*, 1988; *Lloyd et al.*, 1990; *Rees et al.*, 1990; *Wu et al.*, 2003]. Also, radar measurements of lower thermospheric winds have been available since the 1980s [e.g., *Johnson and Luhmann*, 1985; *Manson et al.*, 1988, 1989, 1999; *Chang and Avery*, 1997; *Tsuda et al.*, 1999]. These ground-based measurements have indicated that the MLTI dynamics are controlled by tides and gravity waves and that magnetospheric effects are also significant at times. Measurements from satellites began with observations from the Fabry-Perot interferometer on Dynamics Explorer (DE-FPI) [*Hays et al.*, 1981]. The DE-FPI instrument made optical measurements of winds in the altitude range 100–140 km using the 557.7 nm emission [*Killeen et al.*, 1992]. These observations from within the geomagnetic polar cap were found to be in good general agreement with predictions from two numerical thermosphere general circulation models. Subsequent observations made by the High Resolution Doppler Imager (HRDI) [*Hays et al.*, 1993] and by the Wind Imaging Interferometer (WINDII) [*Shepherd et al.*, 1993] on the Upper Atmosphere Research Satellite (UARS) have been used to study more detailed characteristic features of the global circulation at mesospheric and lower thermospheric altitudes [*Morton et al.*, 1993; *Shepherd et al.*, 1993; *Hays et al.*, 1994; *Wu et al.*, 1995; *Burrage et al.*, 1995a, 1995b *McLandress et al.*, 1996; *Wang et al.*, 1997; *Khattatov et al.*, 1997a, 1997b; *Yudin et al.*, 1998; *Huang and Reber*, 2003, 2004; *Cierpik et al.*, 2003; *Forbes et al.*, 2003, 2004]. The UARS measurements have provided important information on migrating tides, nonmigrating tides, and planetary waves. For example, *Burrage et al.* [1995b] were able to determine characteristics of the long-term variability of the solar diurnal tide using HRDI measurements and *McLandress et al.* [1996] used combined HRDI and WINDII measurements to resolve the migrating diurnal and semidiurnal tides in the mesosphere and lower thermosphere. Recently, *Cierpik et al.* [2003] extended these combined measurements and assimilated ground-based data to address the longitude variability of the solar semidiurnal tide in the lower thermosphere.

[4] Despite the progress made using the combination of ground-based and UARS measurements, there are many unanswered questions concerning fundamental processes governing the MLTI mean state and variability. For example, the role of the gravity waves in the dynamics of this region is still not well understood and the time series of tidal observations need to be extended to resolve important seasonal and decadal effects. Also the unambiguous characterization of specific tidal structures is severely limited by aliasing of the measurements from individual spaceborne platforms due to limited local time sampling. Although there are many upper-atmosphere neutral wind measurements from the ground, these measurements are geographically sparse [*Pancheva et al.*, 2002]. Space-based instrumentation augment the ground-based observation network by routinely providing a global view of the complex and evolving dynamics of the MLTI region. While there are some similarities between TIDI and the HRDI and WINDII instrument capabilities, TIDI coverage extends the time series of observations from UARS and provides wind measurements at higher latitudes, yields more altitude coverage during the night, and measures vector winds over a broader swath of local times.

[5] The TIDI observations are also important in that they serve to further constrain the more sophisticated and comprehensive current numerical models of the region. Several lines of modeling and observational evidence have implied that dynamics of the mesosphere are closely coupled to variations in the stratosphere. Significantly, there are new indications that changes in the mesosphere may precede variations in the stratosphere [*Liu and Roble*, 2005]. This is contrary to the traditional view that the mesosphere passively responds to variations in the atmospheric regions below it. These results could imply that the mesosphere may be the trigger for changes in the stratosphere and show the complex nature of coupling within the middle atmosphere and the importance of understand the entire atmosphere as a complete system. New modeling efforts such as the Whole Atmosphere Community Climate Model (WACCM) will allow a better understanding of these connections [*Sassi et al.*, 2004]. Detailed, long-term measurements of the wind structures within the MLTI represent a crucial element for furthering our understanding of the atmosphere as a whole.

[6] The TIMED mission and the TIDI instrument were designed to provide global coverage of the wind field in this region, with a 100% duty cycle, pole-to-pole coverage, and an extended local time measurement swath. A detailed description on how the TIDI instrument measures the neutral wind velocity vector is therefore necessary for current and future scientific studies based on these observations. This paper provides such a description of the instrument and the associated data analysis methodology and presents current research results using TIDI data.

2. Instrument Description

[7] TIDI is a Fabry-Perot interferometer designed to investigate the dynamics of the Earth's mesosphere and lower thermosphere-ionosphere (MLTI) from an altitude of 70 to 120 km. The TIDI interferometer (or Profiler) measures the horizontal vector wind field with a vertical resolution of ∼2 km with accuracies that approach 3 m/s. The design is discussed in detail by *Killeen et al.* [1999] and the early mission performance is presented by *Skinner et al.* [2003]. TIDI is a limb viewer that observes emissions from OI at 557.7 nm and rotational lines in the O_2 (0-0) Atmospheric band at 762 nm to determine the Doppler shift and hence the wind. Some of the key TIDI parameters are shown in Table 1.

[8] TIDI is derived from other space flight Fabry-Perot interferometers designed and built at the University of Michigan. The Dynamics Explorer Fabry-Perot Interferometer (DE-FPI) was a single-etalon instrument designed for observations of emissions from the thermosphere [*Hays et al.*, 1981]. The High Resolution Doppler Imager on the Upper Atmosphere Research Satellite (HRDI/UARS) was a triple-etalon Fabry-Perot system designed for observations of the stratosphere, mesosphere, and lower thermosphere (10–120 km) [*Hays et al*, 1993; *Grassl et al.*, 1995]. The TIDI instrument uses designs and concepts developed in these programs while incorporating new ideas and technologies.

Table 1. TIDI Parameters

Parameter	Value
Spacecraft altitude	625 km
Orbital inclination	74.1°
Time to precess through 24 hours of local time	120 days
Instrument mass	41.8 kg
Electrical power	19.32 watts (orbit average)
Data rate	2494 bits/s
Altitude resolution	2 km
Spectral range	550−900 nm
Operational temperature	$20 \pm 5°C$ for profiler −80°C for detector −20°C to 40°C for telescopes
Plate material	Fused silica (Supersil−B)
Post material	Zerodur
Plate diameter	10.5 cm
Coated area diameter	8.6 cm
Gap thickness	2.2 cm
CCD	SITe ST-005AB
CCD size	2000×800 (1000×400 quadrant used)
Pixel size	15×15 microns
Telescope type	Off-axis Gregorian
Clear aperture	7.5 cm
Focal length	17.0 cm
f number	2.27
Nominal horizontal field of view	2.5 degrees
Nominal vertical field of view	0.05 degrees
Scan range	$\pm 5°$ from nominal 20.35° below horizon
Fiber optics	fused silica, Poly Micro Inc.
Core diameter	40 microns
Cladding diameter	56 microns
Numerical aperture	0.22
Number of fibers per field	∼390

[9] TIDI consists of three major subsystems: four identical telescopes, a Fabry-Perot interferometer with a CCD detector, and an electronics module (Figure 1). Light from the selected regions of the atmosphere is collected by the telescopes which are fiber-optically coupled to the detection optics. Each of the four fields of view is spatially scrambled by the random distribution of the fibers in the bundle. A fifth field from a calibration deck is combined with the others so the input to the profiler consists of an array of five concentric circular 90-degree wedges. This input is expanded and collimated for transmission through a selected narrowband filter to isolate the required spectral line. The light is further expanded and collimated for transmission through a Fabry-Perot etalon and is finally imaged onto the CCD via a Cassegrain telescope and a circle-to-line interferometer optic (CLIO) device [*Hays*, 1990]. The TIDI CCD is a SITe model ST-005AB which is a high quantum efficiency, low noise detector. The CCD is passively cooled to about −80°C to reduce dark signal and effects of cosmic radiation. Because of the telescopes and calibration lamps are connected to the profile through optical fiber, the fiber bundle pattern is apparent in calibration and four telescope fields on the detector. Two telescopes are required to form a wind vector since the telescopes have no azimuth adjustment. The same volume of the atmosphere is viewed from orthogonal measurements made about 9 min apart. The four telescopes permit vector winds to be measured along two tracks on either side of the spacecraft. This has the advantage of allowing two local times to be sampled at

the same latitude for low and middle latitudes while also providing complete pole to pole coverage.

## 3. Instrument Operations and Data Reduction
3.1. Anomalies and Remediation
3.1.1. Elevated Background Levels
[10] Shortly after launch, the TIDI instrument signal was observed to have a high and variable background count rate during daytime observations. It was determined through analysis that the background was caused by a light leak on the radiator side of the profiler. Light from the Sun-illuminated Earth is able to reach the TIDI detector through the baffle system intended to exclude it while maintaining thermal isolation. The variation in the background is highly
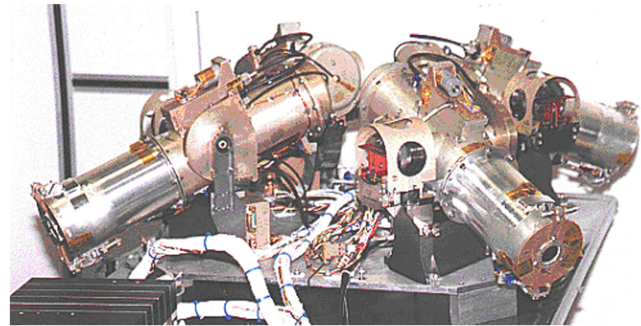
(a)
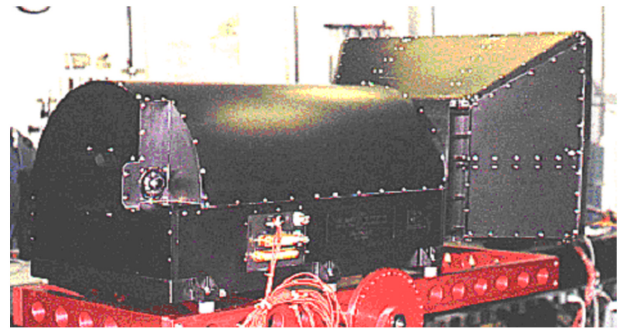
(b)

(c)

Figure 1. Three major TIDI subsystems: (a) the four telescopes, (b) profiler, and (c) the electronics module.
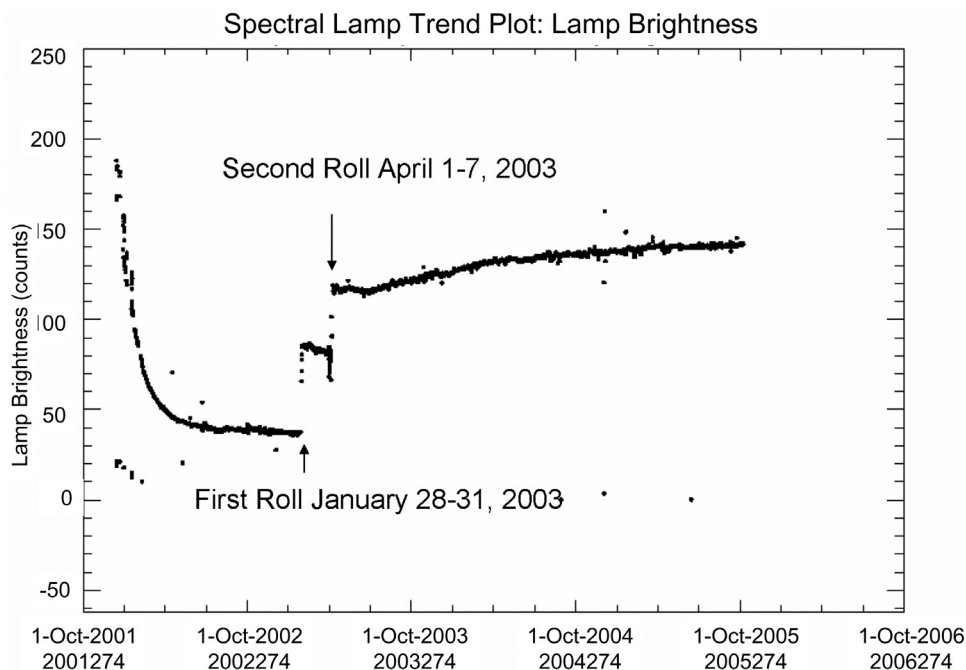
Figure 2. Neon lamp intensity since the launch of the TIMED satellite. The intensity is a reflection of the optical throughput of TIDI, which was affected by the ice formation on the optical surfaces. The initial drop in throughput right after launch is apparent. The sharp increases associated with the two roll maneuvers are also clearly shown.

correlated with albedo features of the Earth below such as clouds. In order to measure and subtract this variable background, samples are obtained periodically by closing the shutters on all telescopes. The distribution function across the detector is represented in terms of empirical orthogonal functions (EOF), which are calculated from a large collection of background samples. The background at any given time is obtained by interpolation of the EOF amplitudes of sampled backgrounds before and after and then subtracted from the total signal to obtain the corrected airglow spectrum. These procedures have been implemented into the daily data production software; see Appendix A for more details.

[11] While the background can be removed from the signal, the added statistical noise remains, which affects overall wind measurement error. To reduce the effect of the high background, the TIDI operational mode also includes additional measurements using the O_2 (0-0) P branch broadband filter. Because this filter is wide enough to allow most of the P branch rotational lines to pass through, the broadband spectral signal is much stronger than that of the P9 or P15 filters. Stronger signal can greatly reduce the effect of the high background. On the other hand, the broadband data are potentially affected by changes in the rotational line distribution due to temperature variation. To determine the rotational temperature of the O_2 (0-0) band, the operational mode includes rotational line measurements (P9 and P15) in both the daytime and nighttime modes of TIDI. The rotational temperature measurement will be incorporated into the broadband data processing.

3.1.2. Ice Formation on the Detector Optical Surfaces

[12] Immediately after launch, the throughput of the instrument showed a rapid decrease, which stabilized after a few months. The instrument also showed broadening of the spectral distribution and elevated cross-talk between different telescope fields on the detector. Analysis determined that the decrease of throughput and the increase of cross-talk are caused by ice forming on the detector housing window or optical surfaces, which are held at low temperatures ($<-60°C$) by the thermal control system. Because the detector is cooled by a passive radiator and equipped with only small-capacity heaters, this system cannot warm its detector housing to a temperature high enough to sublimate the ice by itself. The radiator points to space during normal flight conditions. To raise the detector housing temperature, the TIMED satellite performed two roll maneuvers in early 2003 (28–31 January, 1–7 April 2003) during which the radiator was turned toward the warmer Earth surface. Consequently, a large percentage of the ice was removed, throughput increased, and cross-talk was greatly reduced [*Skinner et al.*, 2003]. Figure 2 displays the entire history of the TIDI optical throughput using neon calibration lamp intensity variations, which include the rapid drop right after launch and sharp increases associated with the two roll maneuvers. As shown in this figure, the throughput is slowly improving over time. From Day 300 of 2002 to Day 300 of 2003, the LOS wind errors have reduced by 30% due to the ice reduction from the two roll maneuvers.

3.2. Observational Modes

[13] TIDI measures neutral winds by limb-scanning different altitudes using several airglow emissions. Currently, the TIDI instrument samples an altitude range from 70 to 120 km during the daytime (Figure 3) and from 80 to 103 km at night (Figure 4). Figure 3 shows the scan steps in a time and altitude display, with different colors
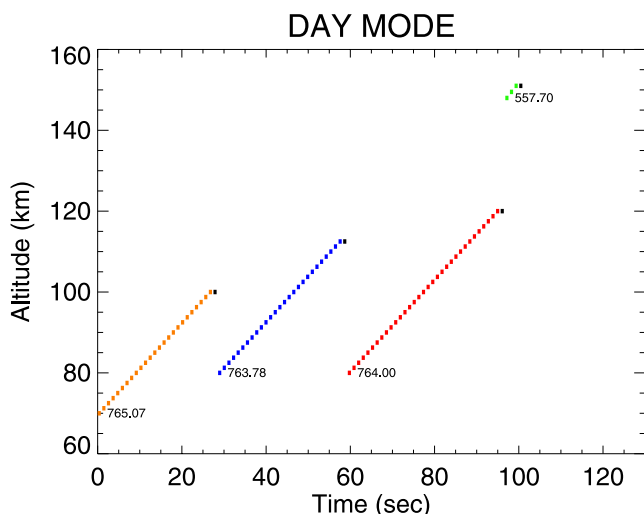
Figure 3. Daytime mode for TIDI. The mode contains sampling steps for four emissions: O_2 (0-0) P15 765.07 nm (orange), O_2 (0-0) P9 763.78 nm (blue), O_2 (0-0) broadband 764.00 nm (red), and O 557.7 nm (green). The integration times for the steps are 0.75 second. Background sampling steps are marked by black color.

representing the various filters employed. The three O_2(0-0) band filters are P15 (765.07 nm), P9 (763.78 nm), and broadband (764.00 nm). The daytime mode also includes a few samples of the O 557.7 nm (green) at high altitudes. Background samples with the shutters closed are also performed. All daytime samples have an integration time of 0.75 second. The altitude step size for the three O_2 (0-0) band filters is 1.25 km. The step size for the O 557.7 nm emission is 1.5 km. Figure 4 shows the current nighttime mode for the TIDI instrument. The night mode also includes the three O_2 (0-0) band filters P9 (763.78 nm, 3-s exposure), P15 (765.07 nm, 3-s exposure), and broadband (764.00 nm, 1-s exposure). The mode also includes O 557.7 nm emission samples (green). The altitude step size is 2.5 km for all emissions. Three background samples are also taken (black). The scan cycles for both day and night last about 100 s, which translates into roughly 7 degrees along-track horizontal resolution. The current modes are compromises among different objectives, which include (1) reasonable horizontal resolution, (2) good vertical resolution (1.25 km for daytime; 2.5 km for nighttime), (3) good statistics for each sampling step, and (4) all three O_2 (0-0) band filters are included for rotational temperature evaluation. Overall, these modes meet all the measurement goals.

3.3. TIDI Data Processing Method

[14] The retrieval of winds from TIDI is accomplished through a nonlinear fit of a forward model to the measurements. The forward model parameters include the atmospheric profiles of wind, temperature, volume emission rate, and Rayleigh scattered background which are simultaneously recovered as part of the standard data processing, and also several parameters that describe the state of the instrument. The backgrounds due to the light leak were removed before the nonlinear fit. The procedure for modeling and subtraction the light leak backgrounds are described in

Appendix A. Appendix B presents the formulation of the measured signal (C) obtained on a particular channel (i). In addition to the light leak, TIDI signal was affected by scattering of light out of the intended optical path due to frost on the window of the detector housing. Therefore the formulation of C incorporates a "cross-talk" matrix (T) designed to model the frost scattering. To obtain vertical profiles, C is expressed as a path integral along the LOS, whose terms depend upon the forward parameters and various instrument parameters introduced in Appendices A and B. The inversion of C is accomplished by linearizing the forward model about an initial state, and applying a constrained nonlinear least-squares fitting method [*Rodgers*, 1976]. The LOS integral formulation and details of the inversion are described in Appendix C.

3.4. Calculation of Vector Winds

[15] There are two schemes to calculate the vector winds from TIDI measurements. As has been mentioned earlier, the TIDI samples two sides of the satellite. For each side, the two telescopes will sample the same location 9 min apart as the satellite moves along its orbit at 625 km altitude. More importantly, the two telescopes view the same region from nearly orthogonal directions, which allow measurements from two viewing directions to be decomposed into meridional and zonal wind components.

[16] One way to calculate the vector is to simply pair the sampling locations of one telescope with nearest neighbors from the other telescope. The distance between the two sampling locations should be less than 500 km. The pair of samples is then used to calculate the meridional and zonal wind components at the first telescope sampling location. If no pairing sample can be found, then no vector winds are
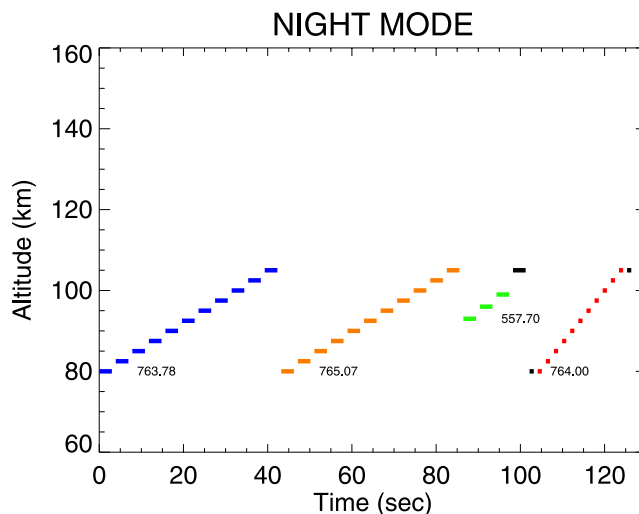

Figure 4. Nighttime mode. The mode contains sampling steps for four emissions: O_2 (0-0) P15 765.07 nm (orange), O_2 (0-0) P9 763.78 nm (blue), O_2 (0-0) broadband 764.00 nm (red), and O 557.7 nm (green). The integration times for the steps are 1 s for broadband and 3 s for all others. Background sampling steps are marked by black color. The altitude range is reduced for the night due to narrowness of the nightglow emission layers. Longer integration is used to increase the signal level.
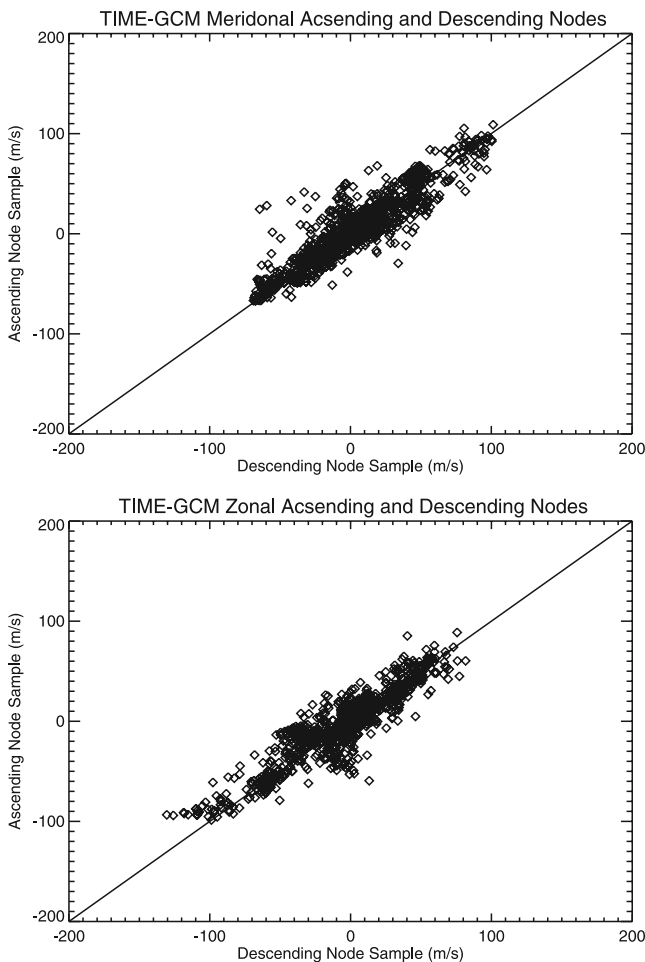
Figure 5. The comparisons between ascending and descending nodes of the TIDI sampled TIME-GCM meridional and zonal winds at 90 km (60–52°N). The good agreements show that the zonally averaged neutral winds at same local time and latitude are roughly the same, even they are sampled a few days apart.

calculated. The second way to calculate the vector winds is as follows. First, the samplings from each telescope are linearly interpolated at evenly spaced track angle grid points. Then the meridional and zonal winds are calculated at these evenly spaced track angle grid points. The neutral winds data provided by NCAR/HAO data processing center (http://timed.hao.ucar.edu/tidi) uses the former method, while the University of Michigan data processing center (http://tidi.engin.umich.edu) uses the latter. The production software for decomposing the TIDI winds is called VEC-TOR. More information about the TIDI data products are provided in Appendix D.

3.5. Zero Wind Position Determination

[17] Since TIDI has four telescopes, there are four zero wind positions to be determined for the LOS winds before they can be used for calculating the vector winds. Four equations are needed to solve for four unknowns. The way to set up the equations is to assume that the neutral wind at the same latitude and same local time should be the same. Owing to the precession of the satellite orbit, the TIDI

telescopes will view the same latitude locations at the same local time during the ascending and descending nodes of the flight. Samples from these two nodes are made from different viewing angles on different days. To verify the assumption about neutral winds being the same, we sampled the TIME-GCM output of meridional and zonal winds at 100 km from 60°N to 52°N according to TIMED orbits and compared the ascending and descending node results (zonally averaged to reduce the nonmigrating tide and planetary wave effects). The results are shown in Figures 5. The two data sets show very good consistency implying the assumption is mostly valid. By linking the ascending and descending node measurement values, the zero wind positions for the four telescopes can be obtained.

4. Preliminary Results

4.1. Wind Measurements

[18] TIDI is designed to study the mesosphere and lower thermosphere dynamics by monitoring the neutral wind in this region. One of the most prominent dynamic features in the MLT region is the mesospheric tide. Figure 6 displays the TIDI vector winds taken at 90 km from the ascending and descending nodes of the both warm and cold sides of the TIDI track. The data from the 15 orbits of during the day are displayed. The common features in all orbits are probably due to migrating tides, whereas other interorbit variations are probably related to planetary waves or non-migrating tides.

[19] TIDI preliminary data were analyzed using daily zonally averaged results to extract the diurnal tides. Zonally averaging the data reduces the contribution from the non-migrating tides and planetary waves and enhances the migrating and zonally mean wind signals in the data. The zonally averaged winds have error of ~7 m/s during the day and ~15 m/s during the night. An example of the zonally averaged data is shown in Figure 7. Figure 7a is for the ascending node (nighttime) data, which are shown in four panels for meridional and zonal winds from the warm and cold sides, respectively. Figure 7b is for the descending node (daytime), which is in the same format as Figure 18a. The meridional winds (left side) from the warm and cold side (upper and lower) show clear antisymmetric features about the equator. That is due to the most dominant migrating diurnal tide (1, 1) mode. On the descending node there are periodic vertical variations with wavelength close to about 20 km (Figure 7b). The zonal winds show more symmetric features near the equator, which is a combination of the zonal mean wind, diurnal tide, and possibly the semidiurnal tide. Even though the diurnal tide feature is strong in the daily zonally averaged meridional wind data plot, the data have only limited local time coverage. To enhance the diurnal tide feature, we calculated the differences between the ascending and descending nodes of the neutral wind measurement and show the results in Figure 7c. The diurnal tide features have doubled their amplitudes (200 m/s peak-to-peak). The zonal wind features are less clear, possibly due to some bias in the zonal wind data.

4.2. Migrating Tides

[20] The TIMED satellite precession rate determines that the TIDI sampling track will cover 24-hour in local time
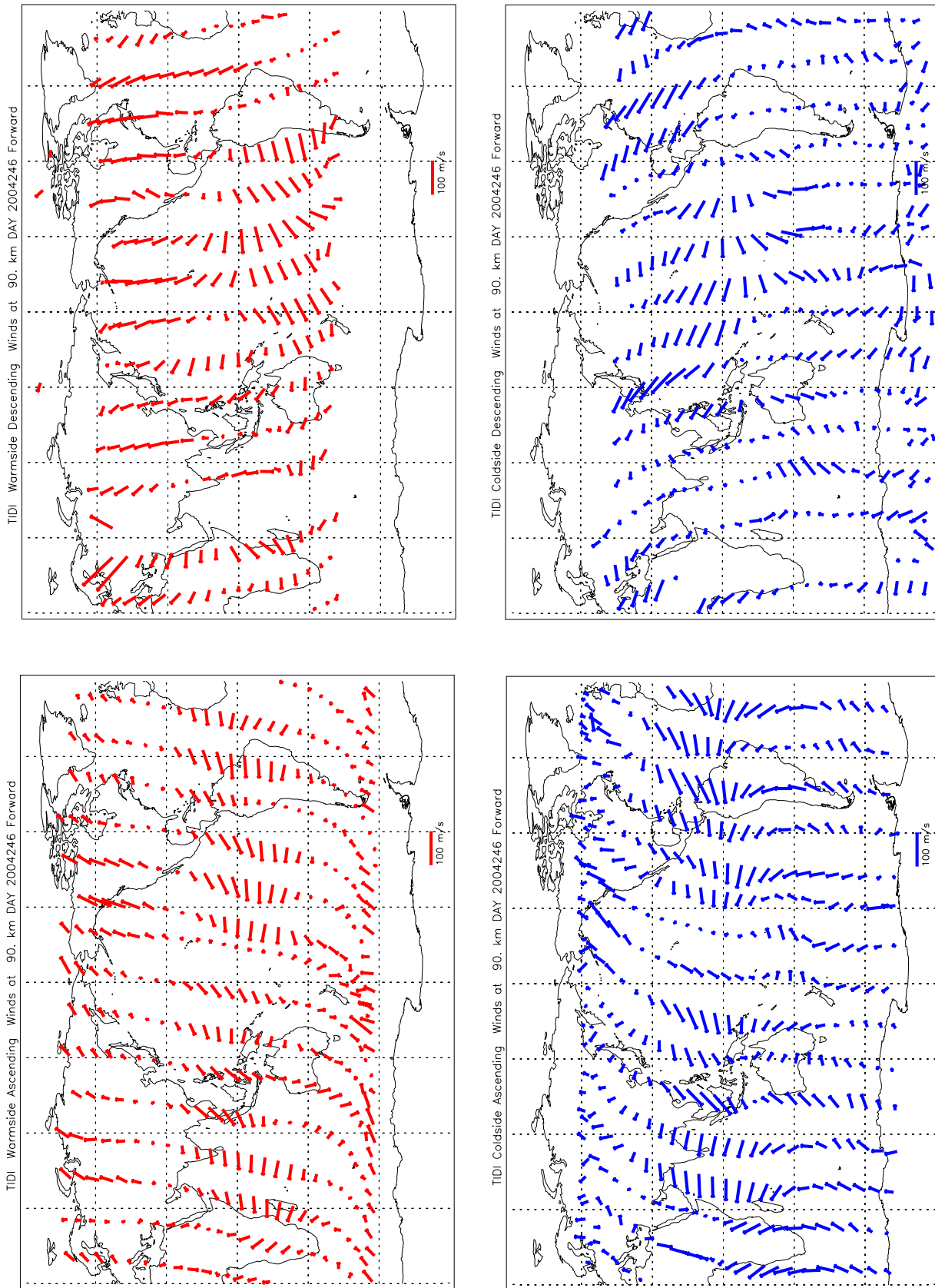
Figure 6. Vector winds at 90 km from (left) ascending and (right) descending nodes of the warm (red) and cold (blue) sides of the TIDI track.
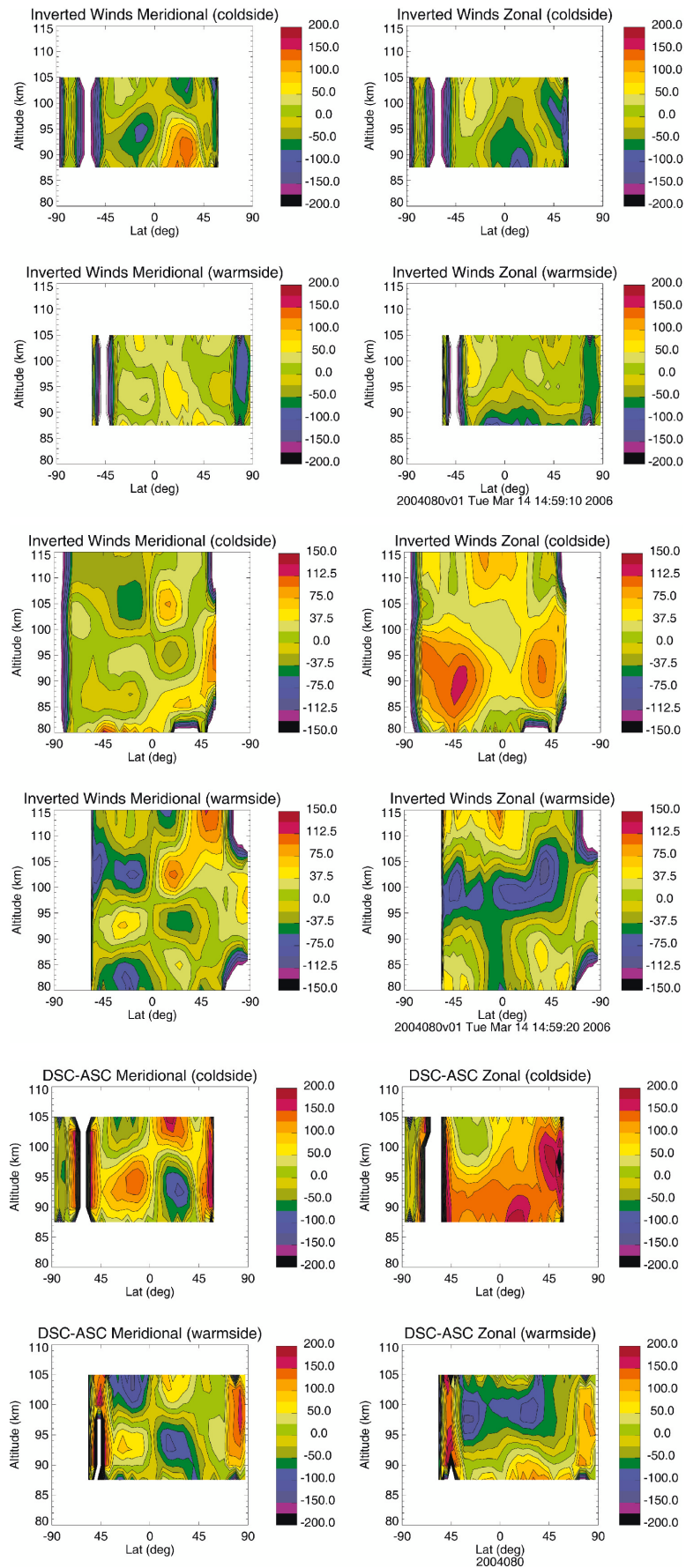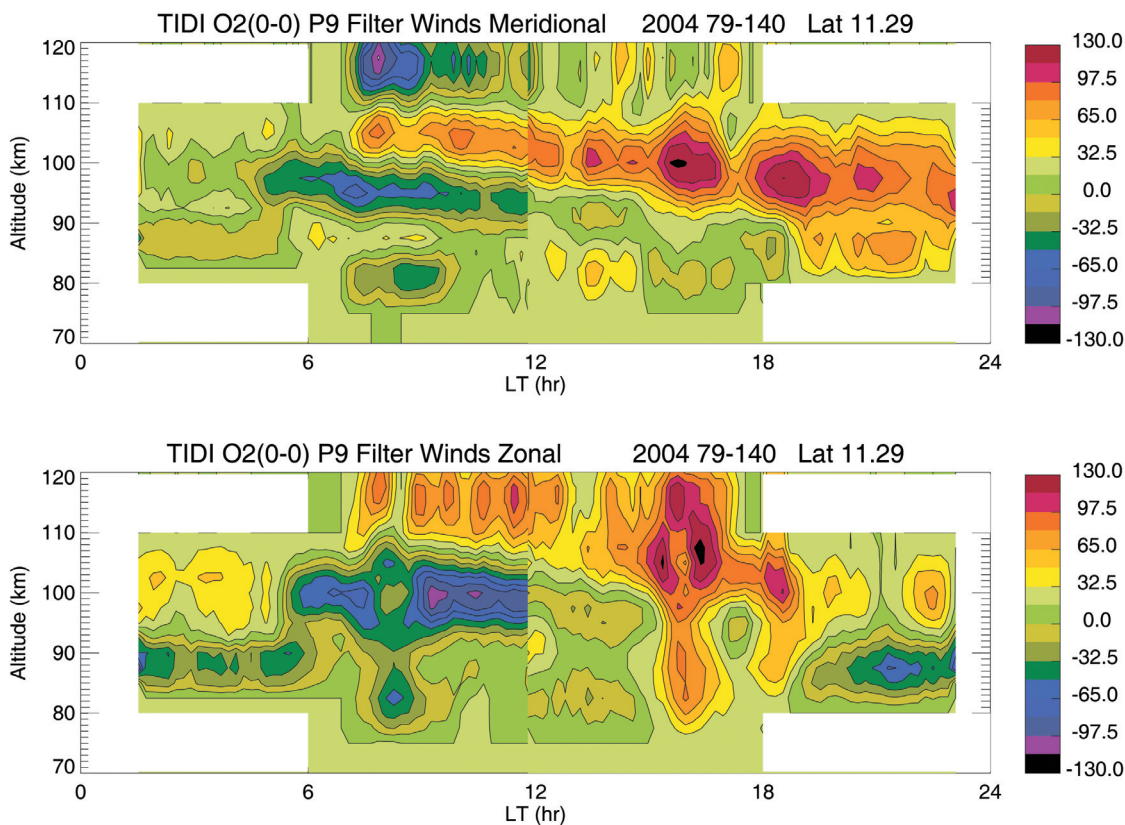
Figure 7

Figure 8. Local time variation of the (upper) meridional and (lower) zonal wind during a 60-day yaw period which covers the 24-hour local time at 11. deg latitude. The variation is consistent with a diurnal variation. The discontinuity near 1200 LT is due to the fact the data on the two sides are 60 days apart. Data near the 0600 LT and 1800 LT usually have large uncertainties due to the breakdown of horizontal homogeneity.

every 60 days, which is one yaw period. Hence we analyzed tides based on individual yaw period. Such analysis is based on the assumption that the tidal amplitudes and the mean wind did not change significantly during the 60-day periods. Therefore the results from this kind of the analysis should be viewed as an average over the 60 days. An example of the 60-day composite 24-hour local time variation at latitude 11°N is shown in Figure 8. The meridional wind (upper panel) shows a clear positive and negative region with a slope in local time, which is consistent with a diurnal tide variation. The discontinuity at 1200 LT in the zonal winds is due to the fact the data on the two sides are 60 days apart. The data near the terminator (0600 LT or 1800 LT) are less reliable. Because of the breakdown of horizontal homogeneity, the inverted results may have large uncertainties. We should point out that TIDI samples a larger nighttime altitude range than previous instruments. The UARS HRDI instrument designed for daytime upper stratospheric winds, observed only one altitude during the night (at 95 km).

[21] The daily zonally averaged meridional winds at 90 km from the years 2003 and 2004 are displayed in

Figure 9. Figure 9a is for the year 2003. The upper panel is for the sampling track that reaches the South Pole and the lower panel is for the one over the North Pole. Figure 9b is for 2004. These plots give an overview of the long-term variations of the meridional winds. Since the TIDI sample is local-time limited, the variations are combinations of the tidal phase changes (due to change in sampling local time) and day-to-day variations. The meridional winds have clear antisymmetric feature near the equator, which is migrating diurnal tide. The feature is particularly strong around day 60 and day 244, consistent with seasonal variation of the diurnal tide. The features related to the diurnal tide appear to be stronger in 2004 near the spring season. By using a least squares fit with a background wind, diurnal, and semidiurnal oscillations, we estimated the meridional diurnal and semidiurnal tide amplitudes and phases for a 60-day interval (79–140) which will have the 24-hour local time coverage. The results are shown in Figure 10. The diurnal tide amplitude and phases are shown in the two panels on the left side, while those of the semidiurnal tide are shown in the panels on the right side. The observational results are

Figure 7. Zonally averaged (upper) meridional and (lower) zonal winds from the (right) warm and (left) cold side of the TIDI observations on Day 2004080. The ascending node is shown in Figure 7a. The node is on the nightside with limited altitude range of airglow coverage. The descending node is displayed in Figure 7b. The node is on the dayside with wider airglow altitude range. The difference between the two nodes is plotted in Figure 7c.
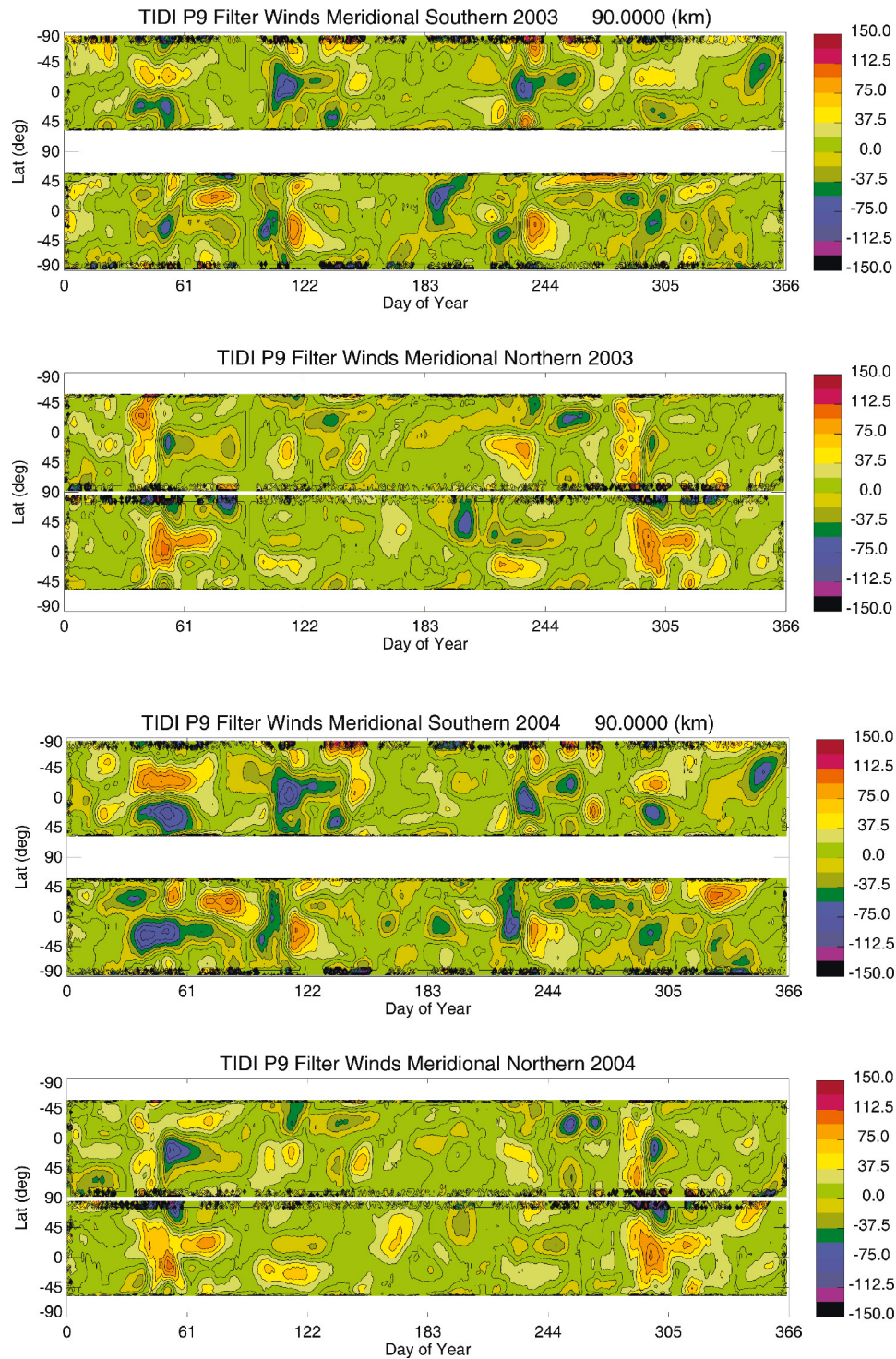
Figure 9. Meridional winds (zonally averaged) at 90 km for (a) 2003 and (b) 2004. The upper panel is for the TIDI track reaches the South Pole and the lower is for that over the North Pole.

compared with GSWM00 results which are plotted in Figure 11 in the same format with the same scale. The similarities can be found between the two in the diurnal tide phases. The migrating diurnal and semidiurnal tide peak at the same latitudes as predicted by the GSWM00 model. The migrating diurnal tide vertical wavelength from the TIDI data are slightly shorter than that predicted by the GSWM00. The peak location of the diurnal tide amplitude is lower than that predicted by the GSWM00. It has been suggested that gravity wave/tide interaction can alter the vertical structure of the tides [*Wu et al.*, 1996]. Gravity wave forcing effects on the tides are still being investigated [*Ortland and Alexander*, 2006].

[22] Estimates of the migrating diurnal and semidiurnal tide amplitude can be obtained each day by fitting a tide and zonal mean model to the TIMED wind and temperature
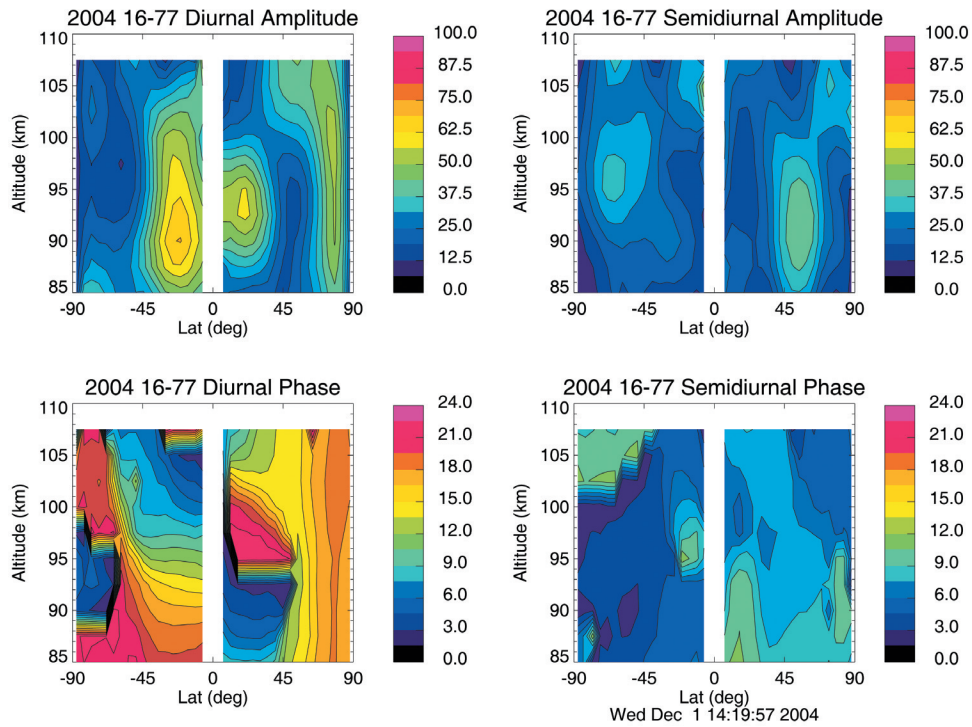
Figure 10. Latitude and altitude variation of the diurnal and semidiurnal tide amplitude and phase over a yaw period (2004 16-77).

data. Both the zonal mean and tide models are represented in terms of a linear combination of basic modal structures. The zonal mean model consists of a set of geostrophic modes that are determined from the zonal mean geopoten- tial which is represented as a two-dimensional expansion in terms of Legendre polynomials. The tide model consists of an expansion in terms of a set of generalized Hough modes. The modes are obtained from tropospheric heating with a
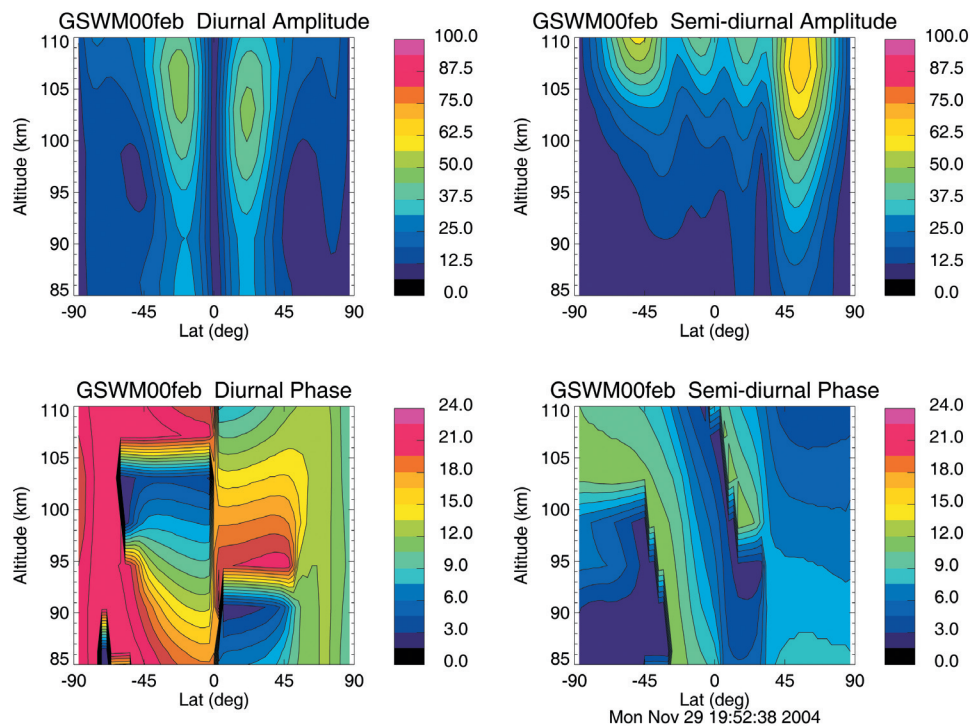

Figure 11. The GSWM00 diurnal and semidiurnal tide amplitude and phase for the month of February. The plot is in the same format as Figure 4 for easy comparison with the TIDI results shown in Figure 4.
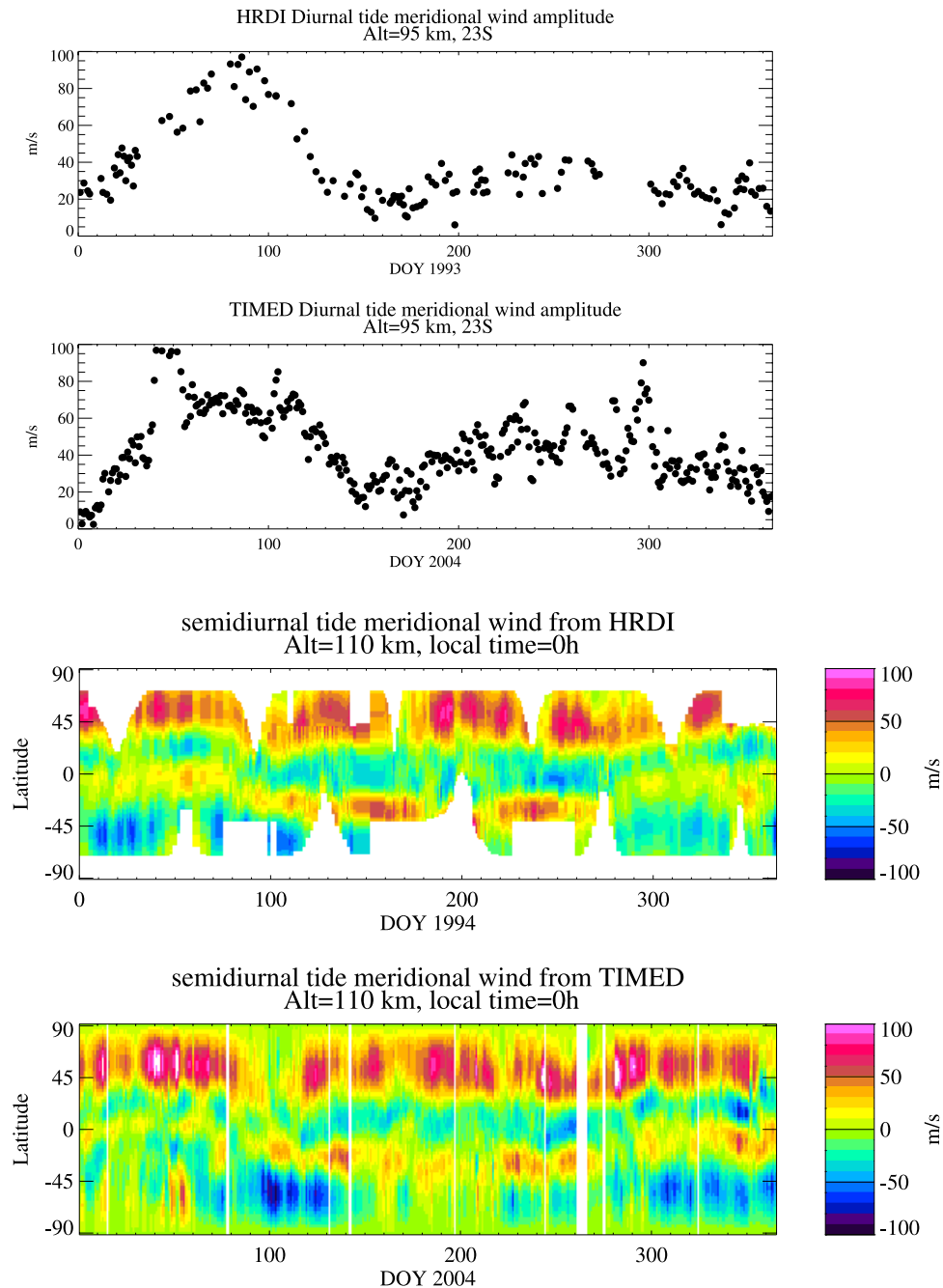
Figure 12. Diurnal tide amplitude (95 km 23°N, 1994 and 2004) and Semidiurnal tide amplitudes at 110 km for 1994 and 2004.

horizontal Hough mode structure. The tide response to the heating is calculated using the model described by *Ortland and Alexander* [2006]. The model includes tide propagation through the zonal mean background, thermal damping, eddy and molecular diffusion, and interaction with gravity waves. The eddy diffusion and gravity wave force are tuned to fit the observed wavelength and amplitude profile of the diurnal tide.

[23] The results of the model fit for each day over the course of one year (2004) are shown in the next several figures. The fit was also performed on HRDI measurements of 1994. The results are represented in Figure 12a, which shows the diurnal amplitude in the meridional wind at 23°S

and 95 km. The diurnal tide amplitude has a strong seasonal variability, which varies in character from year to year. In both the years chosen for the figure, the tidal amplitude has maxima during equinox, with amplitudes much stronger in March, and has minima during solstice. It is also evident from the figure that the tide amplitude can vary substantially on the timescale of a week or two. This variability more likely arises from variability in latent heating, which is a significant source for the nonmigrating diurnal tide.

[24] The estimates for the semidiurnal tide structure are shown in Figure 12b. Since both the amplitude and latitude structure of the diurnal tide varies considerably throughout the year, the figure shows the meridional winds at 110 km
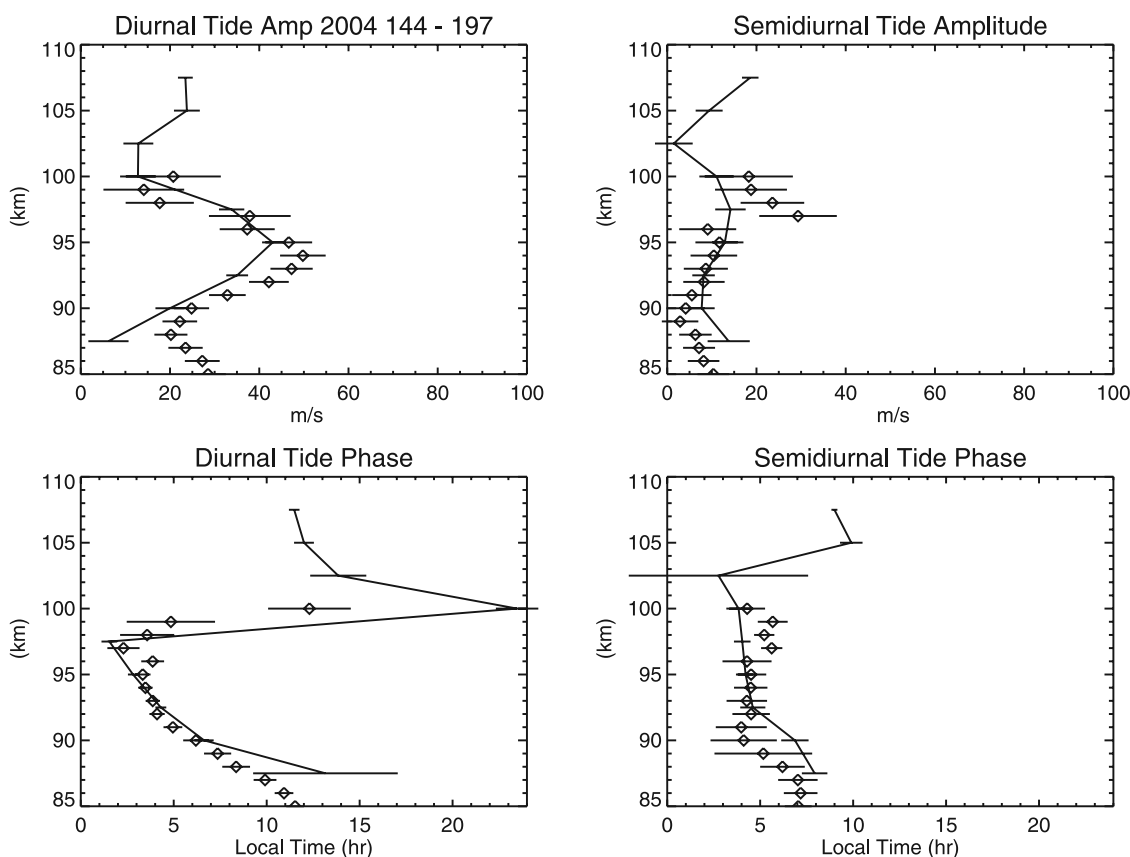
Figure 13. The comparison of (left) diurnal and (right) semidiurnal tide (upper) amplitude and (lower) phase from TIDI (line) and ground-based meteor radar (diamonds) located at Maui. The results from the two measurements show remarkable consistency during this time period.

reconstructed from the tide model at local midnight. Again, results from TIMED are compared to results from HRDI. Note that the HRDI latitude coverage is not global and depends on the latitude range within daylight that is available on one side of the spacecraft or the other. Again we see strong variability on both seasonal and weekly timescales. There is also considerable variability in the location of the nodes in the horizontal structure. Unlike the diurnal tide, which is well represented by the single (1,1) tide mode, the semidiurnal tide must be represented as a combination of several modes. The extent to which each of these modes is excited changes significantly throughout the year. Typically, the meridional wind structure is roughly antisymmetric about the equator. However, midyear, it appears that a tide mode with symmetric meridional wind structure dominates. As a result, strong semidiurnal amplitude in the meridional wind will appear on the equator during boreal summer months. A similar pattern of evolution is observed by both HRDI and TIDI.

4.3. Data Validation

[25] Since HRDI has undergone a long-term validation effort, the good agreement of TIDI with its predecessor lends confidence to the data validity. An additional method used to validate the TIDI measurements is to compare the tidal amplitudes and phase with that obtained from ground-based neutral wind observations. We have compared the diurnal tide and semidiurnal tide amplitude and phase from TIDI to

the measurements from ground based meteor radar located at several sites. We show here the comparison with meteor radar at Maui (22°N) (courtesy of Steve Franke of University of Illinois). The location of the station is ideal because the diurnal tide peaks near that latitude. Hence the two data sets will contain extended neutral wind values. In Figure 13, we show the comparison of diurnal and semidiurnal tide amplitude and phase for 2004 from day 144 to 197. The latitude range is ±5 degrees. The ground based data results were based on multiday composite local time coverage according to the local time of the TIDI overpasses. The TIDI results are from the daily zonally averaged data as shown in Figure 8. We performed simultaneous least squares fitting to both the Maui meteor data and the TIDI data with background wind, diurnal, and semidiurnal tides at different altitudes. The comparison showed remarkable consistency between the two data sets during this time period. This comparison provides an example of our ongoing data validation effort.

5. Conclusion

[26] The TIDI instrument has been in operation since early 2002, providing globally distributed measurements of winds in the mesosphere and lower thermosphere regions of the terrestrial atmosphere. Following two spacecraft maneuvers to warm the instrument and remove ice from the optics during early 2003, the data quality was greatly improved (error reduced by 30%). Together with earlier measurements

from the UARS satellite, a significant long-term record of the dynamics of this region and its interannual variability is being compiled. Owing to the higher inclination of the TIMED orbit, the new data have pole-to-pole coverage during appropriate illumination conditions, enabling measurement of semidiurnal tidal components and detection of geomagnetically driven phenomena. TIDI can measure wind altitude profiles in the night as well as under sunlit conditions, although of course the nightglow emission region has limited vertical extent. Inference of nonmigrating tidal components [*Oberheide et al.*, 2005] has been performed that exploits these data, as well as migrating tidal analysis [*Wu et al.*, 2006]. A new data assimilation model [*Ortland and Alexander*, 2006] has been developed that is capable of revealing the short-term variability of tidal structures, overcoming the inherent limitation of space-based measurements from single spacecraft, the limited temporal pace of local time sampling.

[27] The TIMED spacecraft is in good health, the performance of TIDI mechanical and electrical systems is stable, so an extended life on-orbit is anticipated. This will enable us to address outstanding questions concerning seasonal and interannual variability of mesospheric wind structures and their ability to propagate into the thermosphere, how this process is modulated by tropospheric gravity waves, and how it may be influenced by solar cycle variation and geomagnetic activity. Fine-tuning of data analysis algorithms and calibration of the zero-wind offsets will continue as the challenging task of obtaining consistent long-term wind measurements on-orbit is accomplished. TIDI data is available now through the TIMED mission data center, is of sufficient quality for and validation efforts and collaborative studies, and we look forward to a productive scientific harvest.

Appendix A: Background Subtraction

[28] TIDI measurements are affected by a strong background that is consistent with a light leak in the detector chamber. Consequently, TIDI is now more focused on O_2 (0-0) band emissions included in the day and night modes), but the background level must be determined and subtracted from the measurements before the retrieval can proceed. The background level varies rapidly throughout the orbit, since it is related to the Earth albedo currently beneath the spacecraft. Frequent background observations are made by closing the telescope shutters. A background model (consists of EOFs) is then fit to this background observation. A background model is used as a means of eliminating the random photon count error. This random error is large relative to the size of the spectral signal measured by TIDI. The background $B(i)$ on channel i for a spectrum measurement $C(i)$ made with the telescope open is determined by then interpolating the background models fit at the time of the background observations to the time of the spectrum measurement, and then subtracted from this measurement to obtain the raw spectrum $S(i) = C(i) - B(i)$ with the background removed. The CCD bias is removed from $C(i)$ and $B(i)$; and both are normalized with integration times. Then the random error in the estimate of S is given by:

$$\sigma_S^2 = \sigma_C^2 + \sigma_B^2 = \frac{C}{g\Delta t} + \sigma_B^2 \qquad (A1)$$

where g (e$^-$/count) is the gain and Δt is the integration period. If B is obtained by simply interpolating adjacent background measurements on channel i, then σ_B^2 will be the same order as σ_C^2, thereby effectively increasing the random error of S, which is already large because of the unwanted light-leak background. By fitting a background model that has only eight parameters to the 255 channel background measurement we can effectively reduce the error variance σ_B^2 to zero. The model for the background $B(j)$ on channel j is given by:

$$B(j) = B_0(j) + c_1 B_1(j) + \ldots + c_8 B_8(j) \qquad (A2)$$

where B_0 is the average background observed on a given day and B_i is a background spectral pattern. The background patterns are determined from the covariance matrix for a large sample of background measurements and consist of the first eight eigenvectors (EOFs) of this matrix. The coefficients c_i are determined by performing a least squares fit to each background measurement. Each coefficient is then interpolated to the time of the airglow measurements. The background estimate for each airglow measurement is then reconstructed using the linear expansion of EOFs. These calculations are accomplished in a piece of production software called RETRIEVE.

Appendix B: Calibration of the Forward Model

[29] The TIDI forward model is fit to the spectra obtained by subtracting the background from the measurements. Wind, temperature and volume emission rate profiles can be obtained via inversion once all of the unknown instrument parameters are determined. These parameters are obtained through a least squares fit of the forward model applied to a large number of spectra binned according to the orbital track angle. Every spectra measured at a given position along the orbit track can be assumed to be obtained under roughly equivalent viewing conditions; namely, they all have the same latitude, solar angle, and Doppler shift by Earth rotation. Other geophysical variations that occur in all the spectra that fall in a track angle bin, such as variations in temperature and wind velocity, will only cause an insignificant broadening of the average spectrum so obtained.

[30] TIDI uses a filter that allows six lines in the O_2 (0-0) emission band to reach the detector. The light from the etalon passes through a light-fiber bundle that modulates the brightness of light that lands on the detector pixels. The TIDI instrument is also affected by scattering of light out of the intended optical path due to frost on the window of the detector housing. Two roll maneuvers were performed to raise the detector housing temperature and to melt off most of the frost, with a significant improvement in the TIDI signal. Taking all of these effects into account, the measured signal $C(i)$ obtained on channel i of the detector for a specific telescope is modeled as a sum of a flat background and lines that pass through the filter in the form:

$$C(i) = \sum_k T(i,k) T_{fiber}(i) \big\{ I_{o2} \big[T_{fil}(1) S_1(k)$$
$$+ \ldots T_{fil}(6) S_6(k) \big] + B_{scat} \big\}.$$

The "cross talk" matrix $T(i, k)$ models the frost scattering. For fixed i, $T_k(i) \equiv T(i, k)$ is a function strongly peaked
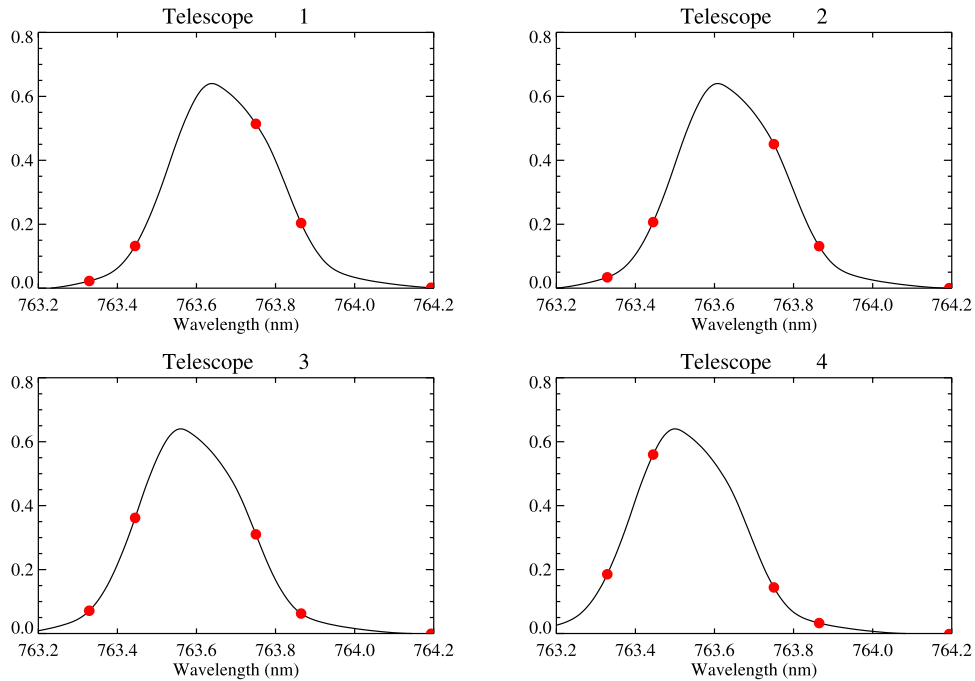
Figure B1. Filter transmission function for each telescope. The center position shifts as a function of telescope due to angle of incidence and spacecraft velocity. The effect on the transmission of four lines is shown with red dots.

at $k = i$. The shape of this function was determined from measurements of white light passing through each separate telescope. The fiber bundle geometry is modeled by normalization constants T_{fiber} which are determined by an instrument calibration procedure. Other variables in this formula are the band strength I_{O2}, the scattering background B_{scat}, the line shape S_j, and the filter transmission T_{fil} (j) for line j. S_j is given by equations (A1) and (A2) without the fiber transmittance, the filter transmittance, and the integration time. The shape and location of each line on the detector that passes through the filter depends on well-known wavelengths of the line center and the line strengths. The shape of the filter function is known, but the wavelength at the center is not because it is very sensitive to the angle of the optical path as it passes through the filter. The reference position, i.e., the position where the fringe pattern is centered when the relative motion of the satellite and atmosphere is zero, is unknown. Other unknown model parameters that are fit to the binned spectra are the band strength, which varies in proportion to the unknown temperature and volume emission rate, the background, the telescope focal length and the etalon gap. The spacing of the fringes of a single line on the detector is very sensitive to the etalon gap and the relative positions of the six lines that pass through the filter are sensitive to the focal length. Figure B1 shows the positions of the rotational lines relative to the filter curve for the four telescopes. Although, there are six rotational lines, only five are plotted because of their relatively large contributions.

[31] A least square fitting method was used to determine the filter shift that can provide the best fit of the forward model to the track angle binned spectral data. The key is to find a filter shift and reference location that would be consistent with spectral line intensities for all four telescope

fields due to the light incident angles and satellite orbital velocity and the Earth rotation speed at various track angles. We should note that the satellite orbital velocity produced different Doppler shifts on different telescopes. The χ^2 map with the filter shift and reference locations of the wind is plotted in Figure B2. We can see clearly a minimum location with reference location near 3000 m/s and filter center position at 763.6 nm.

[32] After the determination of the filter center location and reference position for the neutral winds, the forward model is used to fit the track angle binned spectral data. Such fits are shown Figure B3. Contributions from various rotational lines are plotted in different colors in the lower panels. The combined model spectra are consistent with the measurement data in the upper panels.

Appendix C: Atmospheric Profile Retrieval

[33] We now reformulate the forward model in a way that describes how the measurements by the TIDI instrument depend on atmospheric profiles of wind, temperature, volume emission rate, and a scattering background. The signal $C_i(z_{tan})$ on channel i of the detector when the telescope is pointed with a line of sight of tangent height z_{tan} is expressed as a path integral along the line of sight (LOS) of the sum of a line shape and a background:

$$C_i(z_{tan}) = \int_{z_{tan}}^{\infty} \{K_{\eta,i}(u(z'), T(z'))\eta(z') + B(z')\} \frac{ds}{dz} dz'. \quad (C1)$$

[34] The contribution function $K_{\eta j}$ is a function of the instrument channel i, the wind component $u(z)$ in the LOS direction, and temperature $T(z')$. For O_2 lines, the temper-
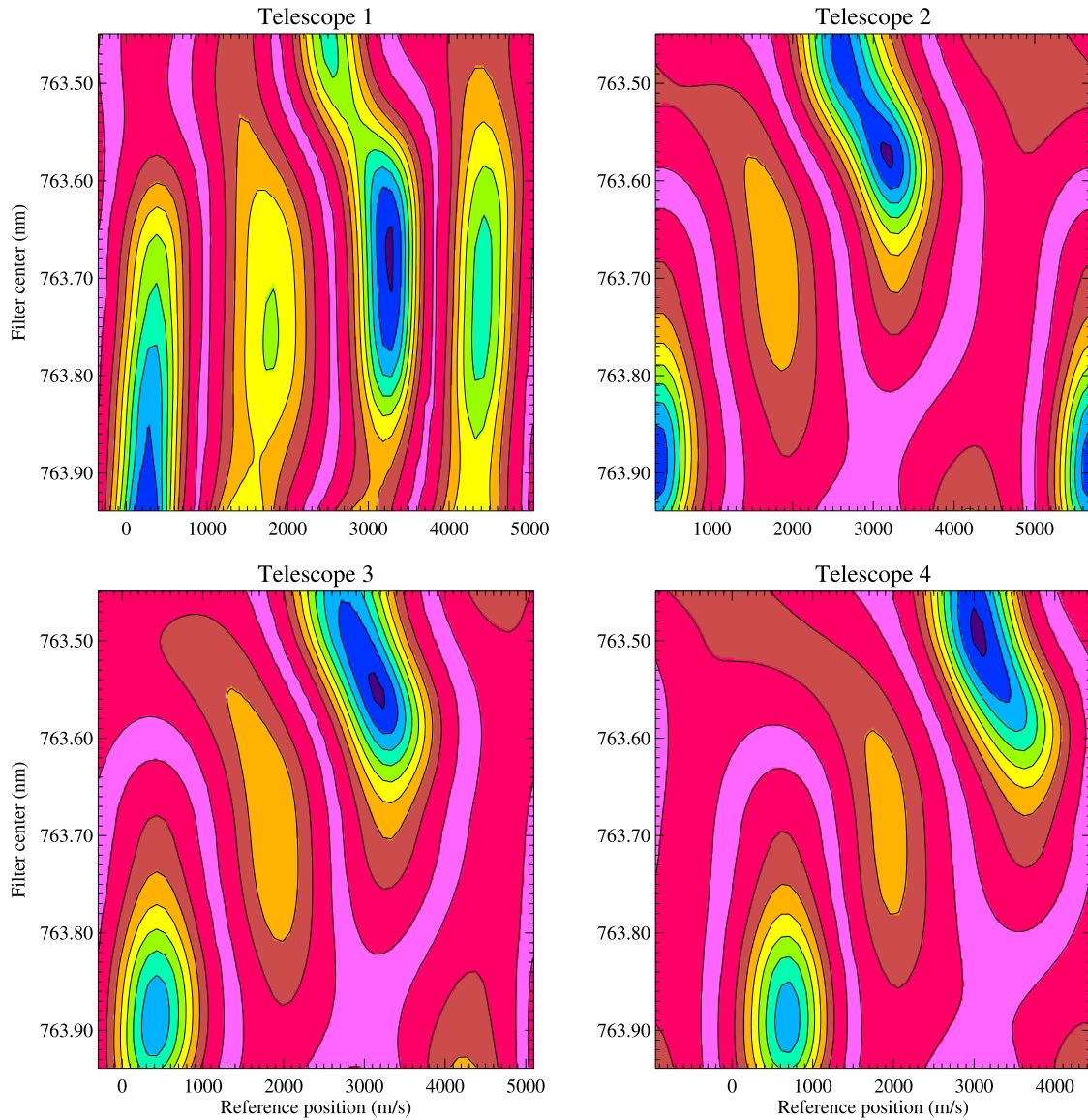
Figure B2. This figure shows the χ^2 of the four-dimensional parameter space given by reference position, filter center, line strength, and background. (Small values are shown in blue, and large values are shown in red). The model is linear in these last two parameters. Each panel shows the minimum χ^2 for a fixed value reference position and filter center. The fit on telescope 1 shows two separate candidates for best fit, but only one of the choices for reference position is consistent for all telescopes. The shift of the filter center is consistent with the expected behavior as a function of incidence angle on the filter and spacecraft Doppler shift.

ature technically has two components, the rotational and Doppler temperature. The contribution function K depends on all the instrument parameters described in the previous section. A detailed description of its determination is beyond the scope of this paper and will be presented elsewhere. The band volume emission rate profile is given by $\eta(z)$ and the background brightness profile is given by $B(z)$. The path length along the LOS is a two-valued function $s(z)$ of height.

[35] Profile inversion is accomplished by first linearizing the forward model about some initial atmospheric state. The initial state is determined by fitting the spectrum measurement at each tangent height to a simple four-parameter model that accounts for brightness, background elevation, line shift, and line broadening. These four line structure parameters are then converted into an effective volume emission rate, background, wind, and temperature, respectively. From the forward model path integral, we obtain the following linearization

$$C_0 + \Delta C = \int_{z_{tan}}^{\infty} \left\{ \left(K_\eta (\eta + \Delta \eta) + (K_u \Delta u + K_T \Delta T)\eta \right. \right.$$

$$\left. \left. + (B + \Delta B)\right\} \frac{ds}{dz} dz'. \right. \tag{C2}$$

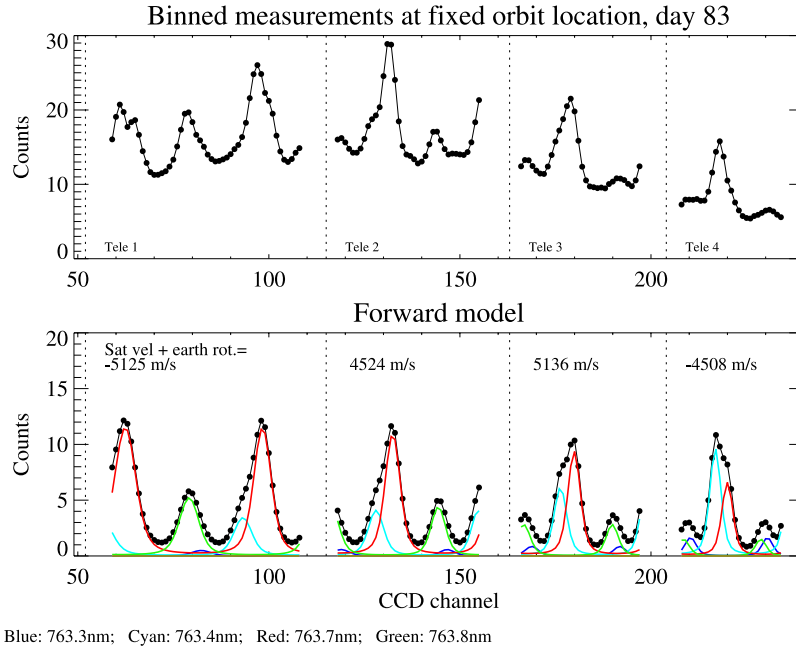Blue: 763.3nm; Cyan: 763.4nm; Red: 763.7nm; Green: 763.8nm

Figure B3. The top panel shows binned TIDI measurements (background contamination removed) on four telescopes. The line shapes consist of a superposition of multiple lines passing through the filter. Note that a single line can produce two fringe patterns on the detector (e.g., the two major peaks on telescope 1 are produced by the same spectral line). The bottom panel shows the forward model fit. The black curve is the sum of the colored curves. The relative contribution of each line was determined by the fit as illustrated in Figures 5 and 6. Note how the line shape differences on each telescope are the result of the changing filter transmissions. In this example, the forward model incorporates normalization constants all equal to 1.

[36] Note that the forward model is nonlinear with respect to wind and temperature. The various kernels K_η, K_u, K_T define how the measured line shape change depends on a change in an atmospheric parameter at a given altitude. For simplicity, we assume that the Doppler and rotational temperature are the same. We next represent the continuous atmospheric profiles as a discrete set of values at the measurement tangent heights and assume the profiles are piecewise linear between these altitudes. Above the top tangent height we assume that the wind, temperature and background profiles are constant, while the volume emission rate is assumed to drop off at an exponential rate. This representation allows the linearized path integral to be expressed as a matrix equation

$$y = y(x_0) + K(x - x_0), \qquad (C3)$$

where $y = (y_1, \ldots, y_n)$ is a vector of measurements, where n is the number of tangent heights and each y_i is a vector of detector measurements with length given by the number of detector channels, $x = (x_u, x_T, x_\eta, x_B)^t$ is a vector constructed from the four different profile representations, x_0 is the vector constructed from the initial guess profile and the matrix kernel $K = (K_u, K_T, K_\eta, K_B)$ is a matrix with four blocks corresponding to each profile.

[37] The profile retrieval is obtained via constrained nonlinear least squares fitting as described by *Rodgers* [1976]. The formula for finding increments to the initial guess that guide the search for a solution through parameter space are derived from the criterion that

$$\chi^2 = (y - y_0)^t S_y^{-1}(y - y_0) + (x - x_0)^t S_0^{-1}(x - x_0), \qquad (C4)$$

must be minimized. The matrix S_y is a matrix with the measurement error variances along the diagonal and

$$S_0 = \begin{pmatrix} \alpha_u J & 0 & 0 & 0 \\ 0 & \alpha_T J & 0 & 0 \\ 0 & 0 & \alpha_\eta J & 0 \\ 0 & 0 & 0 & \alpha_B J \end{pmatrix} \qquad (C5)$$

is the a priori covariance matrix. This matrix typically provides information on profile structure that cannot be determined by the measurement system and can be derived from the statistics of a large body of previous data. Here it is used to simply constrain the small vertical scale structure of the recovered profiles which are typically sensitive to small measurement errors and amplified by the inversion process. This is accomplished by setting each block corresponding to one of the four inverted profiles to a constant times the matrix J given by

$$J_{i,j} = \exp\left(-(i-j)^2/4\right). \qquad (C6)$$

The a priori "covariances" are set to give a very mild constraint: $\alpha_u = 10^4\ m^2/s^2$, $\alpha_T = 10^3\ K^2$, $a_\eta = 2 \times 10^7\ (Ray/cm^{-1})^2$, and $a_R = 10^7\ (Ray/cm^{-1})^2$.

[38] The minimum of χ^2 is found using the formula

$$x_{n+1} = x_0 + S_0 K^t \left(K S_0 K^t + S_y\right)^{-1}(y - y_n - K(x_0 - x_n)), \quad (C7)$$

where the index n gives the Newtonian iteration step. We find that the process converges after five iterations. Constrained inversion has the added benefit of allowing sequential estimation to be employed. Starting with the initial guess $\Delta x_0 = x_0 - x_n$, each individual measurement at a given channel and tangent height can be used to provide an update Δx_i of the increment of x_n obtained at the previous step. The inductive formula for this process is given by:

$$\Delta x_i = \Delta x_{i-1} + S_{i-1} k_i^t (y_i - k_i \Delta x_{i-1}) / \left(k_i S_{i-1} k_i^t + \sigma_i^2\right), \quad (C8)$$

$$S_i = S_{i-1} - S_{i-1} k_i^t k_i S_{i-1} / \left(k_i S_{i-1} k_i^t + \sigma_i^2\right), \quad (C9)$$

where k_i is the row of K corresponding to measurement i and σ_i^2 is the ith diagonal element of S_y. We find this to be more efficient than calculating the inverse of large matrices, since only scalar inversions are required, and is numerically stable. After going through all m measurements, we find $\Delta x_m = x_{n+1} - x_n$. This part of calculation is performed in the production software called INVERT.

Appendix D: Data Products

[39] TIDI data system produces three levels of data. Level 1 is the spectral data from the Fabry-Perot interferometer. The program produces the Level 1 is RETRIEVE. RETRIEVE removes various backgrounds from the raw spectral data. The background due to light leak was estimated based on regularly sampled background data. From the sampled background data, EOF coefficients were estimated and interpolated according to time to construct the background for the spectral data. After the background is subtracted, the spectral data are deconvolved to reverse the diffusive effect of the ice on the detector housing window and optical surfaces. The spectral data were converted form counts to R/cm^{-1}. Moreover, the tangent point latitude, longitude, time, and other information were combined with the spectral data forming the level 1 data. Level 2 data are the inverted line of sight data. Inversion from the spectral data height profile to the geophysical parameters, airglow intensity, Doppler temperature, and line of sight neutral winds profiles was performed by a program called INVERT. The satellite velocity and the Earth's rotational component in the neutral winds are removed during the making of the level 2 data. The inverted data have only one location registration (latitude, longitude, time, etc.) for each profile. Finally, the level 2 data are used to compose the level 3 data by VECTOR, in which the neutral winds are decomposed into the meridional and zonal components. Level 3 data are the highest level data product TIDI data system produces for public use. Currently, TIDI data are been produced at both the University of Michigan and NCAR data sites. The NCAR data site produces not only the neutral winds from the O_2 (0-0) P9 filter but also that from the P15 and broadband filters.

[41] Lou-Chuang Lee thanks the reviewers for their assistance in evaluating this paper.

References

Burrage, M. D., D. L. Wu, W. R. Skinner, D. A. Ortland, and P. B. Hays (1995a), Latitude and seasonal dependence of the semidiurnal tide observed by the high resolution Doppler imager, *J. Geophys. Res.*, *100*, 11,313–11,321.

Burrage, M. D., M. E. Hagan, W. R. Skinner, D. L. Wu, and P. B. Hays (1995b), Long-term variability in the solar diurnal tide observed by HRDI and simulated by the GSWM, *Geophys. Res. Lett.*, *22*, 2641–2644.

Chang, J. L., and S. K. Avery (1997), Observations of the diurnal tide in the mesosphere and lower thermosphere over Christmas Island, *J. Geophys. Res.*, *102*, 1895–1907.

Cierpik, K. M., J. M. Forbes, S. Miyahara, Y. Miyoshi, A. Fahrutdinova, C. Jacobi, C. Meek, N. J. Mitchell, and Y. Portnyagin (2003), Longitude variability of the solar semi-diurnal tide in the lower thermosphere through assimilation of ground- and space-based wind measurements, *J. Geophys. Res.*, *108*(A5), 1202, doi:10.1029/2002JA009349.

Cogger, L. L., J. S. Murphree, C. A. Tepley, and J. W. Meriwether (1985), Measurements of the E-region neutral wind field, *Planet. Space Sci.*, *33*, 373–379.

Forbes, J. M., X. Zhang, E. R. Talaat, and W. Ward (2003), Nonmigrating diurnal tides in the thermosphere, *J. Geophys. Res.*, *108*(A1), 1033, doi:10.1029/2002JA009262.

Forbes, J. M., Y. I. Portnyagin, W. Skinner, R. A. Vincent, T. Solovjova, E. Merzlyakov, T. Nakamura, and S. Palo (2004), Climatological lower thermosphere winds as seen by ground-based and space-based instruments, *Ann. Geophys.*, *22*, 1931–1945.

Grassl, H. J., W. R. Skinner, P. B. Hays, M. D. Burrage, D. A. Gell, A. R. Marshall, D. A. Ortland, and V. J. Abreu (1995), Atmospheric wind measurements with the High Resolution Doppler Imager (HRDI), *J. Spacecr. Rockets*, *32*, 169.

Hays, P. B. (1990), Circle to line interferometer optical system, *Appl. Opt.*, *29*, 1482–1489.

Hays, P. B., T. L. Killeen, and B. C. Kennedy (1981), The Fabry-Perot Interferometer on Dynamics Explorer, *Space Sci. Instrum.*, *5*, 395–416.

Hays, P. B., V. J. Abreu, M. E. Dobbs, D. A. Gell, H. J. Grassl, and W. R. Skinner (1993), The High Resolution Doppler Imager on the Upper Atmospheric Research Satellite, *J. Geophys. Res.*, *98*, 10,713–10,723.

Hays, P. B., D. L. Wu, M. D. Burrage, D. A. Gell, H. J. Grassl, R. S. Lieberman, A. R. Marshall, Y. T. Morton, D. A. Ortland, and W. R. Skinner (1994), Observations of the diurnal tide from space, *J. Atmos. Sci.*, *51*, 3077–3093.

Hernandez, G., and J. L. Smith (1984), Mesospheric wind determinations and the P1(2) C, D lines of the X2-PI OH (8-3) band, *Geophys. Res. Lett.*, *11*, 534–537.

Huang, F. T., and C. A. Reber (2003), Seasonal behavior of the semi-diurnal tides and mean flows at 95 km, based on measurements from the High Resolution Doppler Imager (HRDI) on the Upper Atmospheric Research Satellite (UARS), *J. Geophys. Res.*, *108*(D12), 4360, doi:10.1029/2002JD003189.

Huang, F. T., and C. A. Reber (2004), Nonmigrating semidiurnal and diurnal tides at 95 km based on wind measurements from the High Resolution Doppler Imager on UARS, *J. Geophys. Res.*, *109*, D10110, doi:10.1029/2003JD004442.

Johnson, R. M., and J. G. Luhmann (1985), High latitude mesopause neutral winds and geomagnetic activity: A cross-correlation analysis, *J. Geophys. Res.*, *90*, 8501–8506.

Khattatov, B., V. V. A. Yubin, M. A. Geller, P. B. Hays, and R. A. Vincent (1997a), Diurnal migrating tide as seen by the high resolution Doppler imager/UARS: 1. Monthly mean global meridional winds, *J. Geophys. Res.*, *102*, 4405–4422.

Khattatov, B. V., M. A. Geller, V. A. Yubin, and P. B. Hays (1997b), Diurnal migrating tide as seen by the high resolution Doppler imager/UARS: 2. Monthly mean global zonal and vertical velocities, pressure, temperature, and inferred dissipation, *J. Geophys. Res.*, *102*, 4423–4435.

Killeen, M., T. L. B. Nardi, P. N. Purcell, R. G. Roble, T. J. Fuller-Rowell, and D. Rees (1992), Neutral winds in the lower thermosphere from Dynamics Explorer 2, *Geophys. Res. Lett.*, *19*, 1093–1096.

Killeen, T. L., et al. (1999), TIMED Doppler Interferometer (TIDI), *Proc. SPIE*, *3756*, 289–301.

Liu, H.-L., and R. G. Roble (2005), Dynamical coupling of the stratosphere and meosphere in the 2003 southern hemisphere major stratospheric sudden warming, *Geophys. Res. Lett.*, *32*, L13804, doi:10.1029/2005GL022939.

Lloyd, N., A. H. Manson, D. J. McEwen, and C. E. Meek (1990), A comparison of middle atmospheric dynamics at Saskatoon (52 N, 107 W), as measured by a medium-frequency radar and a Fabry-Perot interferometer, *J. Geophys. Res.*, *95*, 7653–7660.

Manson, A. H., C. E. Meek, S. K. Avery, and D. Tetenbaum (1988), Comparison of mean wind and tidal fields at Saskatoon (52N, 107 W), and Poker Flat (65 N, 147 W), during 1983 1984, *Phys. Scr.*, *37*, 169–177.

Manson, A. H., C. E. Meek, H. Teitelbaum, F. Vial, R. Schminder, D. Kurschner, M. J. Smith, G. J. Fraser, and R. R. Clark (1989), Climatologies of semi-diurnal and diurnal tides in the middle atmosphere (70–110 km) at middle latitudes (40–55 degrees), *J. Atmos. Terr. Phys.*, *51*, 579–593.

Manson, A. H., et al. (1999), Seasonal variations of the semi-diurnal and diurnal tides in the MLT: Multi-year MF radar observations from 2 to 70 degrees N, and the GSWM tidal model, *J. Atmos. Sol. Terr. Phys.*, *61*, 809–828.

McLandress, C., G. G. Shepherd, and B. H. Solheim (1996), Satellite observations of thermospheric tides: Results from the Wind Imaging interferometer on UARS, *J. Geophys. Res.*, *101*, 4093–4114.

Morton, Y. T., R. S. Lieberman, P. B. Hays, D. A. Ortland, A. R. Marshell, D. L. Wu, W. R. Skinner, M. D. Burrage, D. A. Gell, and J.-H. Yee (1993), Global mesospheric tidal winds observed by the high resolution research satellite, *Geophys. Res. Lett.*, *20*, 1263–1266.

Oberheide, J., Q. Wu, D. A. Ortland, T. L. Killeen, M. E. Hagan, and R. G. Roble (2005), Nonmigrating diurnal tides as measured by the TIMED Doppler Interferometer: Preliminary results, *Adv. Space Res.*, *35*(11), 1911–1917.

Ortland, D. A., and M. J. Alexander (2006), Gravity wave influence on the global structure of the diurnal tide in the mesosphere and lower thermosphere, *J. Geophys. Res.*, *111*, A10S10, doi:10.1029/2005JA011467.

Pancheva, D., et al. (2002), Global-scale tidal variability during the PSMOS campaign of June-August 1999: Interaction with planetary waves, *J. Atmos. Sol. Terr. Phys.*, *64*, 1865–1896.

Rees, D., A. Aruliah, T. J. Fuller-Rowell, V. B. Wickwar, and R. J. Sica (1990), Winds in the upper mesosphere at midlatitude: First results using an imaging Fabry-Perot interferometer, *Geophys. Res. Lett.*, *17*, 1259–1262.

Rodgers, C. D. (1976), Retrieval of atmospheric temperature and composition from remote measurements of thermal radiation, *Rev. Geophys.*, *14*, 609–624.

Sassi, M., F. D. Kinnison, B. A. Boville, R. R. Garcia, and R. Roble (2004), The effect of ENSO on the dynamical, thermal and chemical structure of the middle atmosphere, *J. Geophys. Res.*, *109*, D17108, doi:10.1029/2003JD004434.

Shepherd, G. G., et al. (1993), WINDII, The WIND Imaging Interferometer on the Upper-Atmosphere Research satellite, *J. Geophys. Res.*, *98*, 10,725–10,750.

Skinner, W. R., et al. (2003), Operational Performance of the TIMED Doppler Interferometer (TIDI), *Proc. SPIE*, *5157*, 47–57.

Tsuda, T., K. Ohnishi, F. Isoda, T. Nakamura, R. A. Vincent, I. M. Reid, W. B. Harijono, T. Sribimawati, A. Nuryanto, and H. Wiryosumarto (1999), Coordinated radar observations of atmospheric diurnal tides in equatorial regions, *Earth Planets Space*, *51*, 579–592.

Wang, D. Y., C. McLandress, E. L. Fleming, W. E. Ward, B. Solheim, and G. G. Shepherd (1997), Empirical model of 90–120 km horizontal winds from wind-imaging interferometer green line measurements in 1992–1993, *J. Geophys. Res.*, *102*, 6729–6745.

Wiens, R., H. G. G. Shepherd, W. A. Gault, and P. R. Kosteniuk (1988), Optical measurements of winds in the lower thermosphere, *J. Geophys. Res.*, *93*, 5973–5980.

Wu, D. L., P. B. Hays, and W. R. Skinner (1995), A least squares method for spectral analysis of space-time series, *J. Atmos. Sci.*, *52*, 3501–3511.

Wu, D., L. P. B. Hays, and R. G. Roble (1996), Doppler imager wind measurements with simulations from the NCAR thermosphere-ionosphere-mesosphere electrodynamics circulation model, *J. Geophys. Res.*, *101*, 19,147–19,160.

Wu, Q., T. L. Killeen, S. Nozawa, D. McEwen, W. Guo, and S. C. Solomon (2003), Observations of mesospheric neutral wind 12-hour wave in the northern polar cap, *J. Atmos. Sol. Terr. Phys.*, *65*, 971–978.

Wu, Q., T. L. Killeen, D. A. Ortland, S. C. Solomon, R. D. Gablehouse, R. M. Johnson, W. R. Skinner, R. J. Niciejewski, and S. J. Franke (2006), TIMED Doppler Interferometer (TIDI) observations of migrating diurnal and semi-diurnal tides, *J. Atmos. Sol. Terr. Phys.*, *68*, 408–417.

Yudin, V. A., M. A. Geller, B. V. Kahttatov, D. A. Ortland, M. D. Burrage, C. McLandress, and G. G. Shepherd (1998), TMTM simulations of tides: Comparison with UARS observations, *Geophys. Res. Lett.*, *25*, 221–224.

————————

D. A. Gell, R. J. Niciejewski, and W. R. Skinner, Space Physics Research Laboratory, University of Michigan, 2455 Hayward Street, Ann Arbor, MI 48109-2143, USA.

T. L. Killeen, S. C. Solomon, and Q. Wu, National Center for Atmospheric Research, High Altitude Observatory, P. O. Box 3000, Boulder, CO 80307-3000, USA. (qwu@ucar.edu)

D. A. Ortland, Northwest Research Associates, P. O. Box 3027, Bellevue, WA 98009-3027, USA.